Towards a mobile quantitative phase imaging microscope with smartphone phase-detection sensors

XIANGJIANG BAO, $^{1,2,^{\star}}$ LUCAS KREISS , 1 JOSH LERNER , 1 AND ROARKE HORSTMEYER, 1,2

Abstract: Quantitative phase imaging (QPI) enables visualization and quantitative extraction of the optical phase information of transparent samples. However, conventional QPI techniques typically rely on multi-frame acquisition or complex interferometric optics. In this work, we introduce *Quad-Pixel Phase Gradient Imaging* (QP²GI), a single-shot quantitative phase imaging method based on a commercial quad-pixel phase detection autofocus (PDAF) sensor, where each microlens on the sensor covers a 2 × 2 pixel group. The phase gradients of the sample induce focal spot displacements under each microlens, which lead to intensity imbalances among the four pixels. By deriving the phase gradients of the sample from these imbalances, QP²GI reconstructs quantitative phase maps of the sample from a single exposure. We establish a light-propagation model to describe this process and evaluate its performance in a customized microscopic system. Experiments demonstrate that quantitative phase maps of microbeads and biological specimens can be reconstructed from a single acquisition, while low-coherence illumination improves robustness by suppressing coherence-related noise. These results reveal the potential of quad-pixel PDAF sensors as cost-effective platforms for single-frame QPI.

1. Introduction

In traditional bright-field microscopic imaging, the optical phase information of a transparent sample cannot be directly measured because standard image sensors record only light intensity and are insensitive to the phase of the optical field. As a result, transparent or weakly scattering samples are difficult to observe, since they absorb little light and produce minimal intensity contrast.

To overcome this limitation, various quantitative phase imaging (QPI) techniques [1,2] have been developed to measure the optical phase of transparent objects. Among them, holography-based approaches [3,4] recover the phase by interfering the sample beam with a coherent reference beam, enabling full-field quantitative reconstruction of the optical path difference. However, these interferometric methods typically require high temporal and spatial coherence of the illumination, precise reference-beam alignment, and vibration isolation, which limit their applicability in compact or cost-sensitive imaging systems. QPI based on the transport of intensity equation (TIE) [5,6] is a non-interferometric method to obtain phase information. The method can be implemented by introducing slight defocus during image acquisition, phase recovery is then performed by solving a partial differential equation relating intensity transport and phase gradients. This requires multi-frame acquisition and is primarily limited to transparent, thin samples. Furthermore, the accuracy of this method strongly depends on precise knowledge of the defocus distance and the system's optical transfer function. Any error in these parameters, as well as noise or sample-induced intensity fluctuations, can lead to significant phase reconstruction artifacts.

Other QPI methods are primarily based on structured or asymmetric illumination, such as quantitative differential phase contrast (DPC) imaging [7–9]. In practice, the phase-gradient

¹Department of Biomedical Engineering, Duke University, Durham, North Carolina 27708, USA

²Ramona Optics Inc., 1000 W Main St., Durham, North Carolina 27701, USA

^{*}xiangjiang.bao@ramonaoptics.com

contrast in DPC is typically obtained by capturing pairs of images under complementary asymmetric illumination patterns. These implementations generally assume the weak-object approximation [10] and derive both absorption and phase transfer functions under partially coherent illumination. Such methods require multi-frame acquisition, and the accuracy of phase recovery strongly depends on the phase transfer function, which is sensitive to the degree of coherence of the illumination. Fourier ptychographic microscopy (FPM) [11, 12] is another illumination-based QPI method which synthesizes a large numerical aperture (NA) in Fourier space and reconstructs both the amplitude and phase information by computationally combining a sequence of low-resolution intensity images captured under varying illumination angles. However, this technique requires multi-frame acquisition and involves a time-consuming computational reconstruction process.

A different popular strategy to obtain phase information is by placing a microlens array (MLA) above the pixels of the sensor, as in a light field microscope (LFM) [13–16] or a Shack–Hartmann wavefront sensor (SHWS) [17–19]. In LFM, the MLA is positioned at the image plane to capture both the spatial and angular information of light rays emerging from the sample. The recorded light field enables numerical reconstruction of both amplitude and phase, at the expense of spatial resolution due to the division of the sensor into sub-apertures defined by individual microlenses. In contrast, SHWS employs the MLA to directly sample the local wavefront slopes by measuring the displacement of focal spots formed by each microlens on the sensor. The local tilt information is then integrated to reconstruct the wavefront phase. SHWS is typically used in adaptive optics, for example, to measure ocular wavefronts in ophthalmology [20, 21], to inspect lens quality [22, 23], or to detect wavefront aberrations caused by atmospheric turbulence [24]. However, it is less suited for direct imaging of complex samples, as the sensor records a map of spot displacements rather than a two-dimensional image of the sample.

Another imaging technique that employs an MLA is the phase-detection autofocus (PDAF) camera [25, 26]. In 2021, OmniVision launched its first image sensor for smartphones (OV50A) with 100% phase-detection coverage [27]. This sensor employs the quad-pixel PDAF technology, in which every 2×2 pixel group is covered by a single microlens, enabling all pixels to participate in phase detection while maintaining full imaging capability. Previous research has revealed the potential of PDAF sensors for 3D imaging [28]. In this work, we investigate the potential of a quad-pixel PDAF sensor for OPI, and introduce *Quad-Pixel Phase Gradient Imaging* (OP²GI), a single-shot QPI method based on a quad-pixel PDAF sensor. Here, P² simultaneously denotes the *Pixel* and *Phase* aspects of the method, as well as the 2×2 pixel structure employed for phase-gradient detection. In this configuration, the local optical phase gradient is inferred from estimating spot displacements under each microlens, which is similar to a conventional SHWS; however, unlike a typical SHWS that uses large microlenses each mapped onto tens or hundreds of pixels, the quad-pixel PDAF sensor integrates a dense microlens array directly on the image sensor, with each microlens covering only four pixels (Fig. 1a). This compact geometry effectively performs wavefront sampling at the image plane, allowing the captured image to retain high spatial resolution after pixel binning while encoding local optical phase-gradient information within each pixel group. The sensor has a pixel width of 1.008 μ m. After binning all pixels within each 2×2 pixel group, the pixel-limited spatial resolution is approximately $4 \mu m/M$, where M denotes the magnification of the imaging system. Leveraging this architecture, our work demonstrates that commercially available quad-pixel PDAF sensors originally designed for smartphone cameras has the potential to serve as a compact, low-cost, and single-shot platform for QPI.

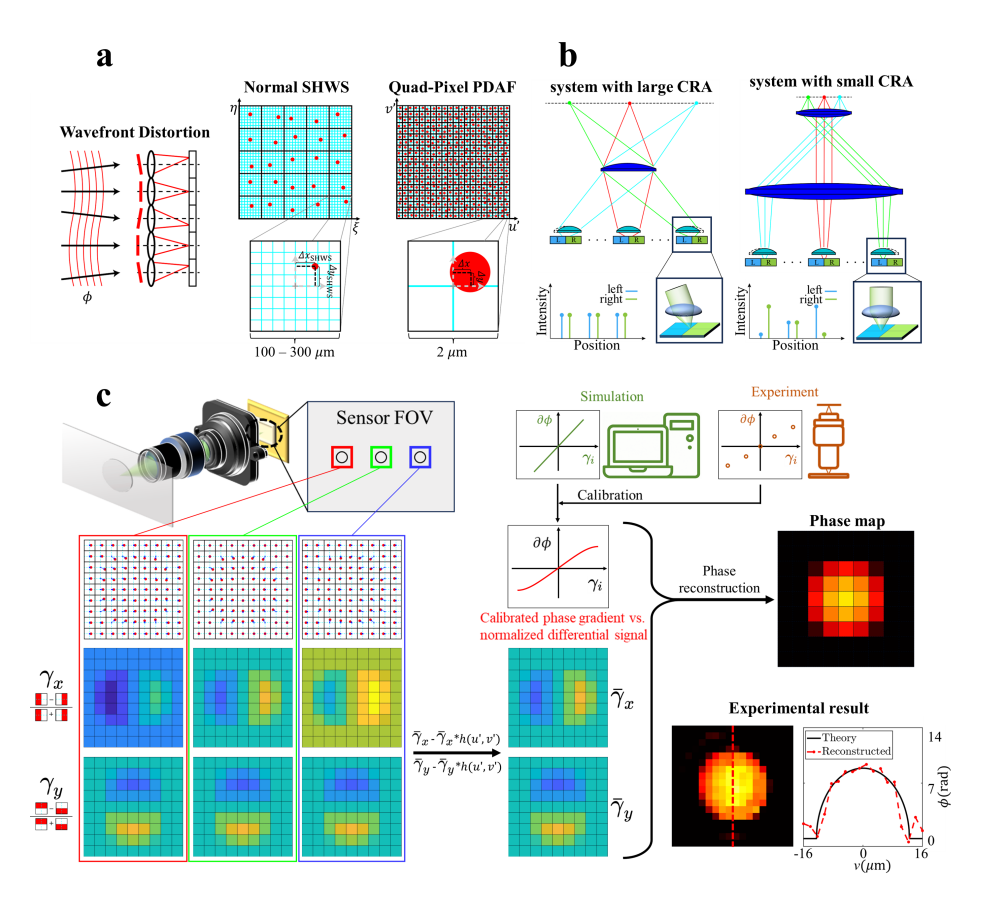


Fig. 1. Illustration of the phase detection principle and workflow of quad-pixel phase gradient imaging (QP²GI).(a) Difference between the phase-detection principle of a common Shack–Hartmann wavefront sensor (SHWS) and a quad-pixel phase detection autofocus (PDAF) sensor. (b) Illustration of the effect of chief ray angle (CRA) mismatch in an imaging system employing a microlens array (MLA) phase-detection sensor. The plots below show the responses of the left and right pixels at different sensor positions. (c) Workflow of QP²GI and the reconstructed phase map of a 25 μ m-diameter microbead immersed in an environment with a refractive-index difference of $\Delta n = 0.03$.

2. Theory and method

2.1. Phase Detection Principle of QP2GI

In this work, the quad-pixel PDAF sensor shares a common underlying principle for optical phase detection with a SHWS: both infer the local phase gradient of the wavefront by measuring the displacement of the focal spot formed beneath each microlens. In essence, a quad-pixel PDAF sensor can be regarded as a simplified SHWS, in which only four pixels are located under each microlens to detect the spot displacement (Fig. 1a). Therefore, it is instructive to first revisit the basic principle of wavefront measurement in a conventional SHWS [17].

Ideally, in a common SHWS, if there is no wavefront aberration, the incident wavefront passes through each microlens and is focused onto the center of the corresponding sub-aperture. In this case, no spot shift is observed at the pixel plane. Here, and throughout this paper, the term *pixel plane* refers specifically to the photosensitive surface. In contrast, when wavefront aberrations exist, the aberrated light is translated into measurable spot displacements (Fig. 1a).

We define (ξ, η) as the coordinates on the pixel plane of a conventional SHWS, The lateral phase gradient introduced by aberrations can then be expressed as:

$$k_{\xi} = \frac{\partial \phi(\xi, \eta)}{\partial \xi}, \quad k_{\eta} = \frac{\partial \phi(\xi, \eta)}{\partial \eta},$$
 (1)

where k_{ξ} and k_{η} are the transverse components of the wave vector \mathbf{k} , whose magnitude is $k = 2\pi/\bar{\lambda}$, with $\bar{\lambda}$ denoting the effective wavelength of light. Here, $\phi(\xi, \eta)$ is the optical phase of the incident wavefront at the microlens plane.

Under the paraxial approximation, the wavefront tilt angles induced by the aberration for each sub-aperture can be calculated as:

$$\theta_{\xi} \approx \frac{k_{\xi}}{k} = \frac{1}{k} \frac{\partial \phi(\xi, \eta)}{\partial \xi}, \quad \theta_{\eta} \approx \frac{k_{\eta}}{k} = \frac{1}{k} \frac{\partial \phi(\xi, \eta)}{\partial \eta}.$$
 (2)

By applying the geometric relationship, the focal spot displacement is given by:

$$\Delta x_{\text{SHWS}} = f_l \theta_{\mathcal{E}}, \quad \Delta y_{\text{SHWS}} = f_l \theta_{\eta},$$
 (3)

Here, the wavefront tilt angles θ_{ξ} , θ_{η} represent the local slope of the wavefront within each sub-aperture, corresponding to the deviation of the propagation direction from the optical axis, and f_{l} denotes the focal length of each microlens. Thus, the phase gradient information can be quantitatively obtained directly from the spot displacement, and the phase distribution of the light field can subsequently be reconstructed from these gradients in different directions.

From the previous derivation, it is essential to accurately determine the position of the focal spot center for a high-quality phase gradient measurement. For a SHWS with multiple pixels under one microlens, a simple way to determine the displacement of the focal spot by its center is to calculate the centroid of the intensity distribution in the focal plane [29, 30]:

$$\Delta x_{\text{SHWS}} = X_c = \frac{\sum_i \sum_j X_i I(X_i, Y_j)}{\sum_i \sum_j I(X_i, Y_j)}, \quad \Delta y_{\text{SHWS}} = Y_c = \frac{\sum_i \sum_j Y_j I(X_i, Y_j)}{\sum_i \sum_j I(X_i, Y_j)}, \quad (4)$$

Here, $I(X_i, Y_j)$ denotes the intensity of the pixel located at position (X_i, Y_j) , with (i, j) representing the pixel indices within the sub-aperture beneath each microlens. The coordinate origin is defined at the geometric center of the pixel group beneath each microlens. X_c and Y_c denote the centroid coordinates of the focal spot formed by each microlens on the pixel plane. They represent the measured positions of the focal-spot centers, which correspond to the spot displacements $\Delta x_{\rm SHWS}$ and $\Delta y_{\rm SHWS}$ relative to the geometric center of the pixel group.

Now we consider a quad-pixel PDAF sensor. To apply this type of sensor for optical phase detection, it can be regarded as a SHWS in which only 2×2 pixels are located beneath each microlens. Each microlens samples a small local image region and focuses the collected light onto its underlying 2×2 pixel group, with a pixel width of $1.008~\mu m$. When local phase gradients are present in the image, they introduce angular tilts in the incident wavefront, which are translated into lateral displacements of the focal spot relative to the pixel-group center. Let $I_{\rm UL}$, $I_{\rm UR}$, $I_{\rm LL}$, and $I_{\rm LR}$ denote the measured intensities at the upper-left, upper-right, lower-left, and lower-right pixels, respectively. In this case, since there are only 2×2 pixels beneath each microlens, Eq. (4) reduces to the following expressions:

$$X_{c} = X_{1} \frac{(I_{\rm LL} + I_{\rm UL}) - (I_{\rm LR} + I_{\rm UR})}{I_{\rm LL} + I_{\rm UL} + I_{\rm LR} + I_{\rm UR}}, \quad Y_{c} = Y_{1} \frac{(I_{\rm UR} + I_{\rm UL}) - (I_{\rm LR} + I_{\rm LL})}{I_{\rm UR} + I_{\rm UL} + I_{\rm LR} + I_{\rm LL}},$$
 (5)

As shown in Fig. 1a, due to diffraction and microlens imperfections, the focal spot is not a perfect point, but instead extends over a significant fraction of the 2×2 pixel region. The focal spot formed in a quad-pixel PDAF sensor occupies a relatively larger portion of the area beneath each microlens compared to a conventional SHWS. This spot size allows detectable intensity variations among the four pixels, enabling phase-gradient sensing with only four pixels. However, it also introduces limitations: Eq. (5) becomes less accurate because (X_c, Y_c) cannot precisely represent the actual displacement Δx and Δy of the extended focal spot, as a 2×2 pixel group cannot fully sample the continuous light field projected onto this area.

To overcome this limitation, we introduce γ_x and γ_y , which represent the differential signals in the horizontal and vertical directions, respectively. Let intensities corresponding to each direction on the pixel group defined as $I_{\text{left}} = I_{\text{UL}} + I_{\text{LL}}$, $I_{\text{right}} = I_{\text{UR}} + I_{\text{LR}}$, $I_{\text{up}} = I_{\text{UR}} + I_{\text{UL}}$, $I_{\text{low}} = I_{\text{LR}} + I_{\text{LL}}$. Taking Eq. (5) as a reference, the differential signals are defined as:

$$\gamma_{x} = \frac{I_{\text{left}} - I_{\text{right}}}{I_{\text{left}} + I_{\text{right}}},
\gamma_{y} = \frac{I_{\text{up}} - I_{\text{low}}}{I_{\text{up}} + I_{\text{low}}}.$$
(6)

It is worth noting that the expressions for γ_x and γ_y in Eq. (6) closely resemble the standard formulation used to describe DPC signals under asymmetric illumination in Ref. [9], where I_{left} , I_{right} , I_{up} , and I_{low} correspond to images acquired with different halves of the illumination aperture being blocked. Ideally, by dividing the total intensity within each pixel group, the differential signal becomes insensitive to uniform attenuation, ensuring that γ_x and γ_y respond primarily to phase-induced intensity asymmetries rather than absorption-related amplitude variations. Therefore, these signals are directly related to the lateral displacement of the focal spot. Mathematically, this relationship can be expressed as a mapping:

$$[\Delta x(u',v'), \Delta y(u',v')] = \mathcal{R}[\gamma_x(u',v'), \gamma_y(u',v')], \tag{7}$$

where $\mathcal{R}(\cdot)$ denotes a response function that maps the focal-spot displacements to the corresponding differential signals. (u',v') denote the global coordinates on the image plane. However, Δx and Δy are solely determined by the sample's phase gradient under the condition that, in the absence of a sample, the focal spot formed beneath each microlens is perfectly centered on the corresponding pixel group, which serves as the ideal reference position. In the following section, we analyze the effect of chief ray angle (CRA) mismatch, which introduces an inherent focal-spot displacement even without a sample.

2.2. Analysis of CRA mismatch

The Quad-pixel PDAF sensor used in this work was originally designed for photographic imaging in smartphones. One key difference between smartphone imaging and microscopic QPI lies in

the CRA of the optical system. While microscopic systems are typically designed with a small CRA to maintain uniform focus and minimize aberrations, the PDAF sensor exhibits a large CRA ($\approx 36^{\circ}$ at edge pixels, as specified by the manufacturer) to support a wide field-of-view (FOV). To accommodate this large CRA, the microlenses are intentionally offset relative to the pixel groups.

As shown in Fig. 1b, this microlens shift allows light entering at a steep angle to still focus near the center of the pixel group. In contrast, when the same sensor operates in a microscopic system with a small CRA, light arriving off-axis cannot be correctly focused on the pixel group centers. On the left side of the sensor, the focal spot formed by each microlens shifts rightward relative to that at the sensor center, whereas on the right side, the focal spot shifts leftward. The CRA mismatch therefore leads to nonuniform pixel responses within each group across the entire sensor FOV, manifesting as a background bias in the differential signals γ_x , as illustrated on the left side of Fig. 1c. The background offset in γ_x gradually increases from negative on the left side of the sensor to positive on the right side, reflecting the opposite directions of the focal-spot displacement. Fig. 3c shows the experimentally measured γ_x curves under a CRA mismatch of approximately 10° for different illumination coherences.

Fig. 4a shows the geometry of focal-spot displacement caused by CRA mismatch for each microlens along the horizontal direction. The red lines originate from the center of the exit pupil of the imaging system and therefore represent the chief rays corresponding to each pixel group. The spot displacement of a pixel group caused by CRA mismatch is given by

$$\Delta x = s_x - f_l \tan(\theta_{r,x}),\tag{8}$$

where s_x denotes the microlens shift in the horizontal direction, and $\theta_{r,x}$ specifically refers to the CRA associated with each pixel group beneath a microlens. From Eq. (8), the spot displacement in the horizontal direction is determined by three parameters: the microlens shift s_x , the microlens focal length f_l , and the CRA $\theta_{r,x}$ associated with the pixel. Among these, $\theta_{r,x}$ is the only parameter determined by the incoming light, whereas the other two are inherent to the sensor design. Additionally, f_l influences the propagation of light after the microlens plane, thereby affecting the shape of the focal spot on the pixel plane. In practice, the microlens deviates from the ideal thin-lens model, and the profile of the focal spot is sensitive to microlens imperfections, which makes it unrealistic to fully simulate light propagation. Therefore, we investigated this relationship by experimentally deriving s_x and f_l , as described later in the experimental section.

From the above analysis, the displacement of the focal spot arises from two factors: the CRA mismatch and the phase gradient of the sample. The contribution from the CRA mismatch appears as a gradually varying low-frequency background (Fig. 3c), whereas the contribution from the sample's phase gradient manifests as a high-frequency signal. To remove the background bias, background subtraction can be applied to the results in Eq. (6), which can be implemented through average filtering:

$$\bar{\gamma}_{x}(u',v') = \gamma_{x}(u',v') - \gamma_{x}(u',v') * h(u',v'),
\bar{\gamma}_{y}(u',v') = \gamma_{y}(u',v') - \gamma_{y}(u',v') * h(u',v').$$
(9)

Here h(u', v') represents the averaging filter kernel, whose size is adjusted according to the fine structural features of the sample. The symbol * denotes the convolution operator. Alternatively, the background can be subtracted by referencing an image acquired under the same optical configuration but without a sample. This process removes the low-frequency background and yields the normalized differential signals $\bar{\gamma}_x(u',v')$ and $\bar{\gamma}_y(u',v')$, which are ideally contributed only by the sample's phase gradient. Instead of the mapping in Eq. (7), which relates the focal spot displacement beneath each microlens to the differential signals, we can now establish a mapping that directly connects the normalized differential signals to the phase gradients of the sample:

$$[d_{u}(u,v), d_{v}(u,v)] = \mathcal{G}[\bar{\gamma}_{x}(u',v'), \bar{\gamma}_{v}(u',v')], \tag{10}$$

where $d_u(u, v)$, $d_v(u, v)$ represent the phase gradients of the sample in the horizontal and vertical directions; (u, v) are the global coordinates on the sample plane; and $\mathcal{G}(\cdot)$ denotes the system response function that maps the focal-spot displacement to the actual phase gradients of the sample.

2.3. Propagation model

To establish the correspondence between $\bar{\gamma}_x$, $\bar{\gamma}_y$ and the actual optical phase gradients d_u , d_v , or equivalently to investigate the mapping $\mathcal{G}(\cdot)$ in Eq. (10), a light-propagation model based on the Huygens–Fresnel principle is developed in this section. In the experimental section, the simulation results derived from this model are further calibrated using experimental measurements, as illustrated on the right side of Fig. 1.

From the previous analysis, in addition to the phase gradient of the sample image, the focal-spot displacement at the pixel plane of the quad-pixel PDAF sensor is also influenced by the CRA associated with each pixel group, as well as by the microlens shift that is originally designed to compensate for this CRA.

Before proceeding further, we first establish the coordinate system for the entire imaging configuration. The global coordinates on the sample plane are denoted as (u, v), and those on the image plane are denoted as (u', v'). For each 2×2 pixel group, the local coordinates within a pixel are represented by (x, y), and the corresponding coordinates on a microlens are represented by (x', y').

Consider a sample with thickness distribution $\beta(u, v)$ and refractive index n_s , immersed in an environment of refractive index n_0 . The optical phase distribution can be expressed as

$$\phi(u,v) = \frac{2\pi}{\lambda_0} (n_s - n_0)\beta(u,v) = \frac{2\pi}{\lambda_0} \Delta n \,\beta(u,v), \tag{11}$$

where Δn represents the refractive-index contrast between the sample and the environment. We now write the full expression to simulate the intensity under each pixel group based on Huygens–Fresnel principle [31]:

$$I(x, y; u', v') = \int_{-a+s_{x}(u', v')}^{a+s_{x}(u', v')} \int_{-a+s_{y}(u', v')}^{a+s_{y}(u', v')} \int_{-a+s_{y}(u', v')}^{a+s_{x}(u', v')} \int_{-a+s_{y}(u', v')}^{a+s_{y}(u', v')} J(x'_{1}, y'_{1}; x'_{2}, y'_{2})$$

$$\times M^{*}(x'_{1}, y'_{1}) M(x'_{2}, y'_{2})$$

$$\times \psi^{*}(x'_{1}, y'_{1}; u', v') \psi(x'_{2}, y'_{2}; u', v')$$

$$\times \Theta^{*}(x'_{1}, y'_{1}; u', v') \Theta(x'_{2}, y'_{2}; u', v')$$

$$\times \exp \left[-j \frac{2\pi}{\bar{\lambda}} (r'_{2} - r'_{1}) \right] \frac{\cos(\theta'_{1}) \cos(\theta'_{2})}{\bar{\lambda}^{2} r'_{1} r'_{2}} dx'_{1} dy'_{1} dx'_{2} dy'_{2}.$$

$$(12)$$

where

$$\psi(x', y'; u', v') = \exp\{-j[d_{u'}(u', v')x' + d_{v'}(u', v')y']\},$$

$$\Theta(x', y'; u', v') = \exp\{-jk[\theta_{r,x}(u', v')x' + \theta_{r,y}(u', v')y']\}.$$

Here, a is the pixel width of the sensor. The microlens width is assumed to match the pixel size, since the microlenses are compactly aligned with each other. $s_x(u',v')$ and $s_y(u',v')$ denote the horizontal and vertical microlens shifts at different positions on the sensor, while $\theta_{r,x}(u',v')$ and $\theta_{r,y}(u',v')$ represent the local CRA of each pixel group in the horizontal and vertical directions, respectively. The terms r_1' and r_2' are the geometrical distances from (x_1',y_1') and (x_2',y_2') to the observation point (x,y), respectively, and θ_1' , θ_2' are the corresponding propagation angles relative to the microlens-plane normal. $d_{u'}(u',v')$ and $d_{v'}(u',v')$ are phase gradients of the sample on image plane. The factors $\psi(x',y';u',v')$ and $\Theta(x',y';u',v')$ denote the phase modulations

introduced by the image phase gradient and the local CRA, respectively. The factor M(x', y') represents the complex transmission of the microlens, modeled here as a thin-lens phase element of focal length f_l . $J(x_1', y_1'; x_2', y_2')$ denotes the mutual intensity on the microlens plane, where r_c is the coherence length. Because $\Theta(x', y'; u', v')$ is derived under the paraxial approximation, the simulation results near the sensor edge may be less accurate.

We define the simulated integrated intensities corresponding to each direction of the 2×2 pixel group as

$$I_{\text{left}}^{\text{sim}}(u',v') = \iint_{\Omega_{\text{left}}} I(x,y;u',v') \, dx \, dy,$$

$$I_{\text{right}}^{\text{sim}}(u',v') = \iint_{\Omega_{\text{right}}} I(x,y;u',v') \, dx \, dy,$$

$$I_{\text{up}}^{\text{sim}}(u',v') = \iint_{\Omega_{\text{up}}} I(x,y;u',v') \, dx \, dy,$$

$$I_{\text{low}}^{\text{sim}}(u',v') = \iint_{\Omega_{\text{low}}} I(x,y;u',v') \, dx \, dy,$$

$$(13)$$

where Ω_{left} , Ω_{right} , Ω_{up} , and Ω_{low} denote the integration domains corresponding to the left, right, upper, and lower halves of the 2×2 pixel group, respectively, on the pixel plane.

In Eq. (12) the microlens is modeled as a perfect thin lens, and the cross-talk effect introduced by CRA mismatch is neglected, which inevitably reduces the accuracy of the model. To partially compensate for these effects, we treat them as a background component within each pixel group, assumed to be proportional to the overall intensity. This contribution is incorporated by multiplying Eq. (6) with a constant term *B*, which accounts for the residual background signal:

$$\gamma_{x}^{\text{sim}}(u', v') = B \cdot \frac{I_{\text{left}}^{\text{sim}}(u', v') - I_{\text{right}}^{\text{sim}}(u', v')}{I_{\text{left}}^{\text{sim}}(u', v') + I_{\text{right}}^{\text{sim}}(u', v')},
\gamma_{y}^{\text{sim}}(u', v') = B \cdot \frac{I_{\text{up}}^{\text{sim}}(u', v') - I_{\text{low}}^{\text{sim}}(u', v')}{I_{\text{up}}^{\text{sim}}(u', v') + I_{\text{low}}^{\text{sim}}(u', v')}.$$
(14)

Although this remains a simplified assumption, it nevertheless allows the simulation to capture the essential behavior of the sensor and to provide useful guidance in understanding its performance in the context of QPI. A more accurate simulation can be performed using the finite-difference time-domain (FDTD) method [32], by incorporating known features such as the microlens shape, microlens shift, and intrinsic stack layers of the pixels. For practical applications, the relationship between γ_x , γ_y and the actual phase gradients can be experimentally calibrated using standard samples with known optical properties, thereby establishing a valid mapping between the differential signals and the corresponding phase gradients for real sensor measurements.

By performing simulation based on Eq. (12), (13), (14), we obtain $\mathcal{G}_{\text{sim}}(\cdot)$, which represents the mapping from $\bar{\gamma}_x^{\text{sim}}$, $\bar{\gamma}_y^{\text{sim}}$ to the phase gradient d_u and d_v . $\bar{\gamma}_x^{\text{sim}}$ and $\bar{\gamma}_y^{\text{sim}}$ are normalized differential signal based on simulation, calculated based on Eq. (9). By using a reference sample with known phase information, the experimentally calibrated mapping $\mathcal{G}(\cdot)$ can be expressed as $\mathcal{G}(\cdot) = C_{\text{cali}} \mathcal{G}_{\text{sim}}(\cdot)$. Now Eq. (10) is written as:

$$[d_u(u,v), d_v(u,v)] = C_{\text{cali}} \mathcal{G}_{\text{sim}} [\bar{\gamma}_x(u',v'), \bar{\gamma}_v(u',v')], \tag{15}$$

where C_{cali} is the calibration coefficient that scales the simulated mapping to match the experimentally measured phase gradient.

Once the calibrated phase gradients $d_u(u, v)$ and $d_v(u, v)$ are obtained from measured $\bar{\gamma}_x(u', v')$ and $\bar{\gamma}_y(u', v')$ by Eq. (15), the phase of the sample can be reconstructed by solving the Poisson equation in the frequency domain using Tikhonov regularization [33]:

$$\phi(u,v) = \mathcal{F}^{-1} \left[\frac{-j2\pi p \, D_u(p,q) - j2\pi q \, D_v(p,q)}{(2\pi p)^2 + (2\pi q)^2 + \varepsilon} \right],\tag{16}$$

where (p, q) denote the spatial-frequency coordinates, and $D_u(p, q)$ and $D_v(p, q)$ are the Fourier transforms of the measured phase gradients $d_u(u, v)$ and $d_v(u, v)$, respectively. The parameter ε is a small regularization constant introduced to stabilize the inversion at low frequencies.

2.4. Analysis of coherence

So far, we have established the principle and model of QP^2GI that illustrated in Fig. 1c. However, for a SHWS where multiple pixels lie beneath each microlens, the spatial coherence of the illumination plays a crucial role in accurate spot localization. Insufficient coherence can lead to a blurred focal spot with reduced contrast, thereby degrading the precision of centroid estimation. In the case of the quad-pixel PDAF sensor, where only a 2×2 pixel group is located beneath each microlens, the spot-size variations induced by partial coherence have an even stronger impact on localization accuracy, potentially compromising the robustness and repeatability of QP^2GI .

To investigate this issue, we simulated the intensity distribution and differential signals as functions of the focal-spot displacement beneath a microlens on a 2×2 pixel group located in the central region of the FOV, based on Eq. (12), (13), (14). When simulating the intensity distribution, no microlens shift was introduced, and the incident light was assumed to be perpendicular to the sensor surface in the absence of a sample. In contrast, when simulating the differential signals as a function of focal-spot displacement beneath the microlens, the integration area in Eq. (13) was shifted to emulate the displacement.

Fig. 2a shows the simulated beam profiles under different illumination coherence conditions, with the distance between the microlens plane and pixel plane set to 1 μ m in this simulation. This distance is estimated from the CRA of the sensor with the assumption that the microlens lateral shift for CRA compensation does not exceed half of the 2 × 2 pixel group, and the experimental procedure used to obtain the precise distance is described later in the experimental section. Strictly speaking, this distance ($\sim 2\bar{\lambda}$, estimated from the center wavelength of the visible spectrum) lies at the border between the radiative and near-field regimes. However, since the microlens contains no sub-wavelength structures and the detector integrates the optical field over finite pixel areas, effectively acting as a spatial low-pass filter, the contribution of the remaining high-frequency near-field components is expected to be negligible in the actual experiment. Therefore, Eq. (12) still provides a useful basis for analysis.

Fig. 2a indicates that when the coherence length of the illumination is larger than the width of the pixel group ($\sim 2~\mu m$), the light can be approximated as coherent during propagation. In practice, LED sources typically have a relatively narrow bandwidth ($\sim 30~nm$) compared to incandescent white light. Thus, the coherence length can be estimated by $r_c = \lambda_0^2/\Delta\lambda$, where λ_0 is the center wavelength and $\Delta\lambda$ is the spectral bandwidth. Under typical conditions, the coherence length of an LED exceeds 2 μm . In this case, the light field within each pixel group can be regarded as fully coherent, and Eq. (12) reduces to the coherent form:

$$I(x, y; u', v') = \left| \int_{-a+s_{x}(u', v')}^{a+s_{x}(u', v')} \int_{-a+s_{y}(u', v')}^{a+s_{y}(u', v')} M(x', y') \psi(x', y'; u', v') \Theta(x', y'; u', v') \right| \times \exp \left[-j \frac{2\pi}{\bar{\lambda}} r' \right] \frac{\cos(\theta')}{\bar{\lambda} r'} dx' dy' \right|^{2}.$$
(17)

Fig. 2b presents the relationship between the spot displacement and the differential signal γ_x under different coherence lengths. The curve of γ_x converges to the fully coherent case once the

coherence length surpasses the pixel width. Moreover, in the regime of small spot displacements ($|\Delta x| < 0.1~\mu m$), the curve remains nearly linear. This provides a reliable basis for subsequent analysis, as the correspondence between spot displacement and the differential signal remains stable when the coherence is sufficiently large. On the other hand, this result also highlights a fundamental limitation of the phase-detection method: once the spot displacement extends beyond the linear regime, it becomes difficult to accurately quantify the relationship between spot displacement and the differential signal.

In conclusion, this analysis shows that when an illumination source with a coherence length larger than the size of a single microlens is used, QP²GI is able to exhibit good measurement repeatability and robustness. It also confirms that within a certain range, a linear relationship exists between the normalized differential signal and the focal-spot displacement, ensuring the stability and consistency of phase-gradient measurements.

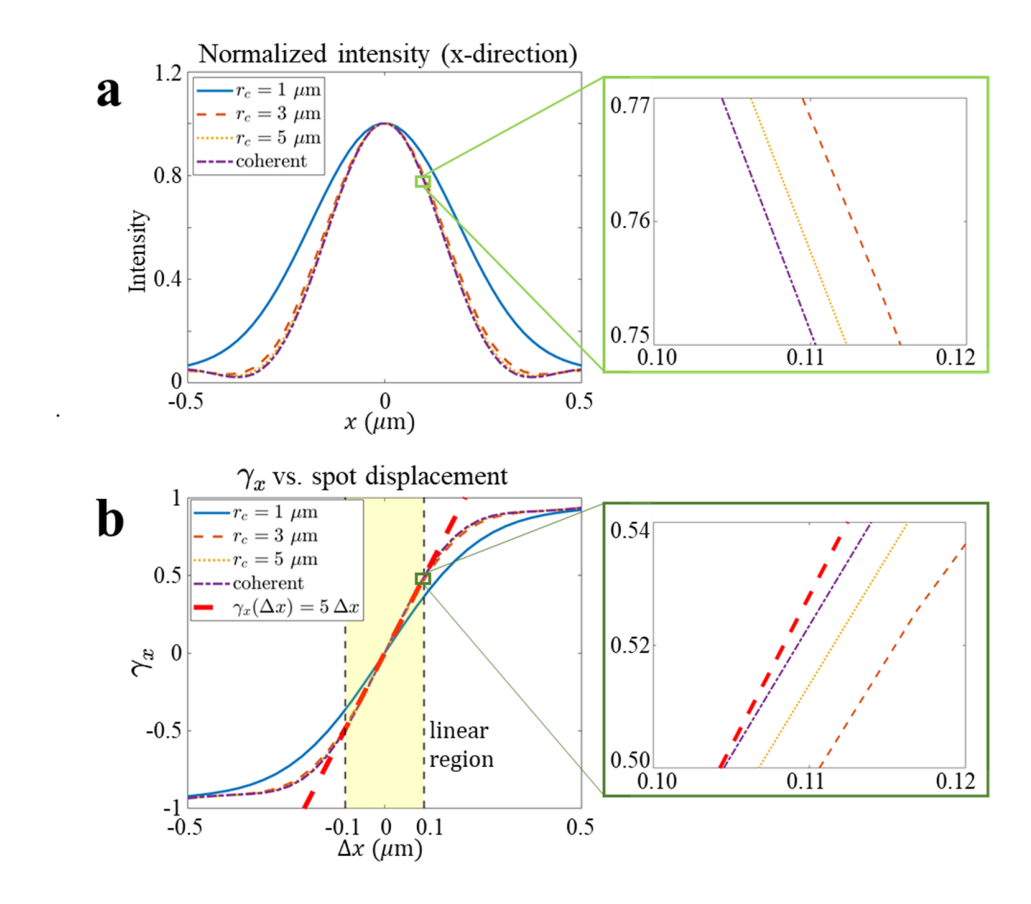


Fig. 2. Simulation results demonstrating the feasibility of optical phase measurement with a quad-pixel PDAF image sensor under different coherence lengths r_c . The incident light is perpendicular to the system and focused onto the center of a 2×2 pixel group. The microlens focal length is set to $f_l=1$ μ m, and the microlens–pixel distance is assumed equal to f_l . (a) Intensity distribution within one 2×2 pixel group along the x direction. (b) Differential signal γ_x as a function of the spot displacement Δx .

3. Experiment

3.1. Experimental setup

As explained above, the large CRA of the quad-pixel PDAF sensor of about 36° poses an inherent challenge for integration with a commercial microscopic system, because the crosstalk induced by CRA mismatch makes it impossible to reliably retrieve the phase gradient of the sample. To investigate the QPI ability of the quad-pixel PDAF sensor, we built a customized optical imaging system along with a tailored illumination module (Fig. 3a). In this system, an inverted CCTV lens (Imaging Lens 1) was placed in front of a flat smartphone lens (Imaging Lens 2) to form a finite-conjugate microscope. Since the CCTV lens has a larger f-number than the smartphone lens, it acts as the aperture-limiting element of the combined system. Therefore, the system's effective NA is constrained by the CCTV lens and can be approximated by its f-number as 0.23. The CRA of this customized configuration was experimentally measured to be 26° at the edge of the sensor. This value was determined by analyzing the correspondence between the illumination angle and the resulting differential signal without a sample, as described in the section detailing the experimental derivation of sensor parameters. Despite the remaining 10° mismatch with the sensor CRA, this system can reliably retrieve the phase gradient of the sample.

The imaging-lens-limited maximum measurable phase gradient can be approximated as $|\nabla\phi|_{\text{max}} = \frac{2\pi}{\bar{\lambda}} \cdot \text{NA}$, which is calculated as 2.73 rad/ μ m at $\bar{\lambda} = 530$ nm. However, because the system was built with two lenses in a finite-conjugate configuration, this value is expected to be smaller in practice, as the sample was not located at the conjugate plane corresponding to the rated f-number of the CCTV lens.

An adjustable iris was placed at the conjugate plane of the diffuser, while the sample was positioned at the conjugate plane of the diffuser's Fourier plane. The illumination thus follows a Köhler-type configuration, in which the coherence of the illumination can be tuned by changing the iris aperture. In the following analysis, we describe the illumination coherence using the parameter $\sigma = NA_{illum}/NA_{obj}$, where NA_{illum} and NA_{obj} denote the NA of the illumination and the CCTV lens, respectively. This convention follows the definition used in QPI under partially coherent illumination, as adopted in DPC microscopy [9].

Fig. 3c demonstrates the image captured using the configuration described in Fig. 3a at different values of σ without a sample. Due to the CRA mismatch, the differential signal γ_x remains nonzero and increases with position even in the absence of a sample, representing the background signal caused by CRA mismatch, as shown in Fig. 1c. It is observed that the γ_x curves at different σ largely overlap, except near the edge of the imaging FOV. This observation is consistent with the discussion of Fig. 2, where the differential signal remains the same with varying coherence as long as the coherence length of the illumination exceeds the size of the pixel group, thereby confirming the repeatability of phase-gradient detection at different coherence levels. The observed drop of γ_x at the FOV edge with decreasing σ may be attributed to reduced spatial coherence in the edge region of the FOV.

3.2. Experimental derivation of sensor parameters

To study the effect of CRA mismatch, we built the setup shown in Fig. 3b. A small light source was placed at the focal plane of a larger lens to collimate the beam, which was then refocused by another lens with an f-number of 1.4. Different CRA conditions of imaging systems can be simulated by moving the sensor forward and backward. The focal spot formed by the second lens can therefore be regarded as the center of the exit pupil of the imaging system. In the experiment, the illumination fully covers the clear aperture of the second lens; therefore, the maximum diverging angle of the beam after the focal spot formed by the second lens is constrained by its f-number.

In Fig. 3d, the differential signals γ_x and γ_y were measured using the configuration shown

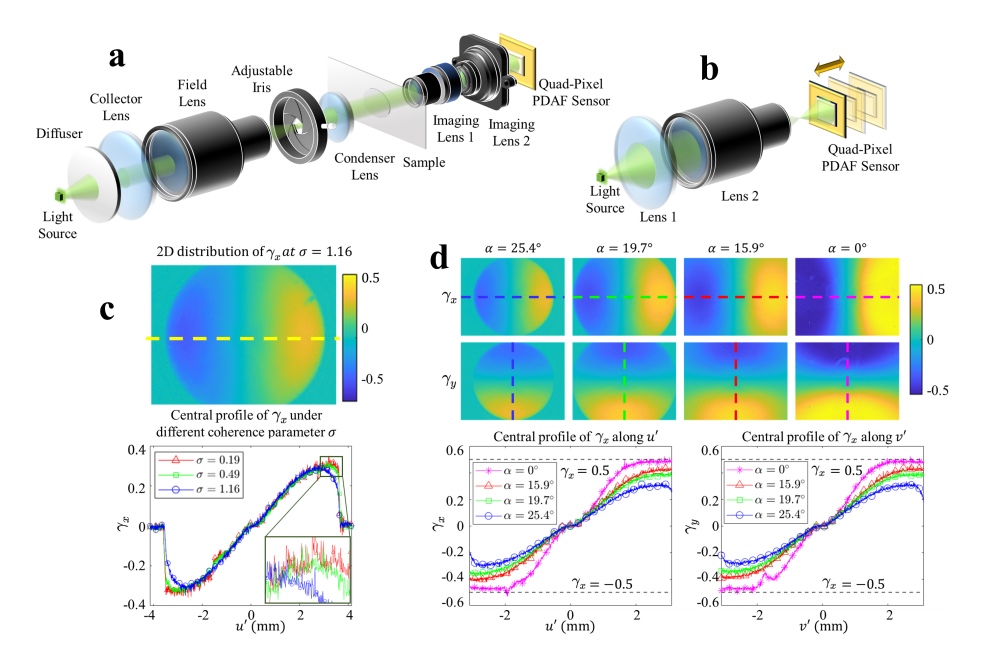


Fig. 3. Experimental setups. (a) 3D schematic diagram of the imaging setup. The light source is a 2 mm \times 2 mm LED centered at 530 nm with a bandwidth of \sim 30 nm. Imaging lens 1 is a CCTV lens with a 2.8 mm focal length and an f-number of 2.2. Imaging lens 2 is a smartphone lens designed for a 1/1.55'' sensor with a measured 8 mm focal length and an f-number of 2. Together, these two lenses form a finite-conjugate imaging system with a measured CRA of 26°. The system magnification M is 2.3. The illumination coherence can be tuned by adjusting the iris. (b) 3D schematic diagram of the setup to simulate different CRAs. After collimation by Lens 1, the beam diameter is expanded to fully cover the clear aperture of Lens 2. The quad-pixel PDAF sensor is positioned beyond the focal plane of Lens 2 and illuminated by the diverging light. Lens 2 has an f-number of 1.4. (c) Differential signal γ_x at different coherence parameters σ , captured by the setup in (a). (d) Horizontal differential signal γ_x and vertical differential signal γ_y captured at different incident angles α with the setup in (b). The maximum differential signal achieved by the system is approximately 0.5.

in Fig. 3b under different incident angles α without a sample. To measure the case of $\alpha=0^\circ$, an additional lens was placed after Lens 2 to collimate the beam. The results show that γ_x and γ_y measured without a sample decrease as the CRA mismatch is reduced. However, it is observed that when $\alpha=0^\circ$, the differential signals converge to 0.5, which is consistent with our assumption in Eq. (14). Due to factors such as crosstalk from CRA mismatch and imperfections in the microlens geometry, γ_x and γ_y cannot reach the ideal value of 1.0 even when the focal spot is fully shifted onto the pixels on one side of a 2×2 pixel group.

To quantitatively estimate the effective focal length f_l of the system, the experimentally measured differential signals γ_x were compared with the theoretical predictions. Three experimental curves of differential signals across the sensor FOV, obtained under different incident angles $\alpha_1 = 15.9^\circ$, $\alpha_2 = 19.7^\circ$, and $\alpha_3 = 25.4^\circ$, are denoted as $\gamma_x^{(1)}(u')$, $\gamma_x^{(2)}(u')$, and $\gamma_x^{(3)}(u')$, respectively. The corresponding exit pupil distances from the sensor plane are labeled as z_1 , z_2 , and z_3 .

Based on the theory presented above, we simulated $\gamma_x(\Delta x; f_l)$ under different microlens focal lengths f_l with perpendicular illumination following a process similar to that used for Fig. 2b,

with the horizontal axis expressed as the focal spot displacement Δx in each 2×2 pixel group. The amplitudes of $\gamma_x(\Delta x; f_l)$ curves are scaled by a factor of 0.5. This scaling factor represents the background term B in Eq. (14) and was determined from the experimental result in Fig. 3b, in which γ_x reaches a maximum of approximately 0.5. By comparing one of the experimental curves, $\gamma_x^{(2)}(u')$, with the corresponding theoretical curve $\gamma_x(\Delta x; f_l)$, the reference focal spot displacement curves $\Delta x^{(2)}(u'; f_l)$ for different focal lengths were determined. In practice, the curve $\gamma_x^{(2)}(u')$ is smoothed to derive the reference focal spot displacement.

From this displacement, the lateral shift of the microlens was calculated as:

$$s_x(u'; f_l) = \Delta x^{(i)}(u'; f_l) + \frac{f_l}{z_i} u', \tag{18}$$

where z_i is the corresponding exit pupil distance from the sensor plane. This formula is derived from Eq. (8) by substituting $\tan(\theta_{r,x})$.

The theoretical curves of the differential signals across the sensor FOV, $\hat{\gamma}_x^{(1)}(u'; f_l)$ and $\hat{\gamma}_x^{(3)}(u'; f_l)$, corresponding to the other two incident angles, were reconstructed from the derived $s_x(u'; f_l)$. Specifically, $\Delta x^{(1)}(u'; f_l)$ and $\Delta x^{(3)}(u'; f_l)$ were first calculated using Eq. (18), and then compared with the simulated $\gamma_x(\Delta x; f_l)$ curve under the corresponding microlens focal length to obtain $\hat{\gamma}_x^{(1)}(u'; f_l)$ and $\hat{\gamma}_x^{(3)}(u'; f_l)$.

Finally, the best-fit focal length f_l was determined by minimizing the difference between the measured and simulated differential signals, expressed as the loss:

$$loss(f_l) = \sum_{u'} \| \Gamma_x(u') - \hat{\Gamma}_x(u'; f_l) \|_2^2,$$
(19)

where

$$\Gamma_{x}(u') = \begin{bmatrix} \gamma_{x}^{(1)}(u') \\ \gamma_{x}^{(2)}(u') \\ \gamma_{x}^{(3)}(u') \end{bmatrix}, \quad \hat{\Gamma}_{x}(u'; f_{l}) = \begin{bmatrix} \hat{\gamma}_{x}^{(1)}(u'; f_{l}) \\ \hat{\gamma}_{x}^{(2)}(u'; f_{l}) \\ \hat{\gamma}_{x}^{(3)}(u'; f_{l}) \end{bmatrix}.$$

The loss reaches its minimum for $f_l = 0.71 \, \mu \text{m}$ (Fig. 4b). Although this is a relatively small distance, it is geometrically reasonable for a sensor designed with a 36° CRA and a pixel pitch of 1.008 μm . If f_l becomes larger, the required microlens shift increases, and the microlens may no longer sufficiently cover the intended pixel within its 2×2 pixel group. Back-side illumination (BSI) techniques [34, 35] can reduce such distances by relocating the metal wiring layers behind the photosensitive region, thereby positioning the photosensitive region closer to the microlens.

The microlens shift $s_x(u'; f_l)$ calculated from Eq. (18) is shown in Fig. 4c as the blue solid line. For comparison, the red dashed line denotes the microlens shift curve calculated directly from the sensor's edge CRA, given by:

$$s_{x}(u'; f_{l}) = \frac{f_{l}}{z_{\text{CRA}}} u', \tag{20}$$

where z_{CRA} represents the distance from the exit pupil to the sensor plane such that the edge light falls onto the center of the edge pixel group. As observed in Figs. 3c, d, and Fig. 4d, γ_x appears flattened in the central region ($|u'| \lesssim 0.12$ mm). This effect is likely due to the fact that the microlenses in the central part of the sensor are not shifted to match the behavior of an actual imaging system, and the focal spot in Fig. 3b is not a perfect point but has a finite geometric size, which results in a uniform light distribution in the central region. The blue solid curve in Fig. 4c illustrates this feature, where s_x exhibits a smaller slope in the central region. The reconstructed $\gamma_x(u')$ curves based on $f_l = 0.71~\mu\text{m}$ are shown in Fig. 4d, and the results exhibit relatively good consistency.

From the above discussion, the differential signals remain nonzero and increase across the sensor even without a sample. This is regarded as a background offset induced by CRA mismatch between the optical system and the sensor that varies across the sensor FOV. The high-frequency signal components originating from the phase gradient can be isolated by subtracting this low-frequency background. In this work, such background is estimated by applying an average filtering to the differential signals as illustrated in Fig. 1c. The resulting signals, which reflect only the phase gradient, are denoted as the normalized differential signals $\bar{\gamma}_x$ and $\bar{\gamma}_y$. Using the estimated f_l and microlens shift s_x , simulations based on Eq. (14) were performed to establish the relationship between the actual phase gradient of the sample and the normalized differential signal at different sensor positions. As shown in Fig. 4e, The relationship between $\bar{\gamma}_x$ and the actual phase gradient of the sample is highly linear at the center of the sensor. Additionally, the same normalized differential signal corresponds to a higher phase gradient at positions farther from the center, indicating that the sensitivity of the sensor to phase gradients decreases with distance from the center.

Although the model becomes less accurate toward the edges of the sensor since the simulated $\gamma_x(\Delta x; f_l)$ curves were derived under perpendicular incidence, we can still regard it as providing important guidance for revealing the fundamental phase detection behavior of the sensor. Additionally, since the overall performance of this model largely depends on the accuracy of the estimated $\gamma_x(\Delta x; f_l)$ curves, a more precise simulation would require detailed knowledge of the microlens shape and arrangement.

3.3. Phase detection and reconstruction results

To test and validate this approach, we imaged polystyrene microbeads (nominal diameter = $25 \mu m$, refractive index $n_s = 1.59$) immersed in an environment with $n_0 = 1.56$ using the imaging system shown in Fig. 3a. Fig. 5 shows the normalized differential signals and the corresponding reconstructed phase maps obtained under different illumination coherence parameters σ . In the figure, the microbeads shown in the three rows correspond to the same microbead in the top bright-field image, captured with only the iris aperture varied.

In our work, the simulated differential signals are obtained from the propagation model based on Eq (14), incorporating the estimated microlens shift and microlens focal length. To match the measured profiles, the simulated curves in Fig. 4e and Fig. 5 are derived by applying a calibration factor of 0.5 to the actual simulation results. The factor was obtained empirically by comparing the simulated phase-gradient amplitudes with the experimental measurements and adjusting the scaling until optimal agreement was achieved. This calibration factor corresponds to C_{cali} in Eq. (15), which indicates that the sensor is less sensitive to the phase gradient than predicted. One possible contributing factor is a shorter distance between the photosensitive layer and the microlens than expected, although achieving such a reduction is challenging in practice. A more likely explanation is that the actual focal spot shape deviates from our simplified model, such that for the same displacement Δx , the resulting normalized differential signal is smaller.

Since the actual phase gradient of the microbeads diverges at the bead edges, the simulation calculates the gradient by applying finite differentiation with a 2 μ m sampling step at the image plane, corresponding to the microlens size of a 2 × 2 pixel group. The normalized differential signals exhibit strong agreement with the simulated results after scaling under low-coherence illumination (σ = 1.16). This confirms the linear relationship between the actual phase gradient and the normalized differential signals at the sensor center, consistent with the simulation. The phase reconstruction is then performed according to Eq. (16), following the workflow shown in Fig. 1c. At σ = 1.16, the reconstructed phase map matches the theoretical prediction. As σ decreases, however, $\bar{\gamma}_x$ and $\bar{\gamma}_y$ become noisier, and the agreement between the reconstructed phase derived from these signals and the ideal spherical gradient shape deteriorates.

Additionally, we investigated this effect for different immersion media in Fig. S1, corresponding

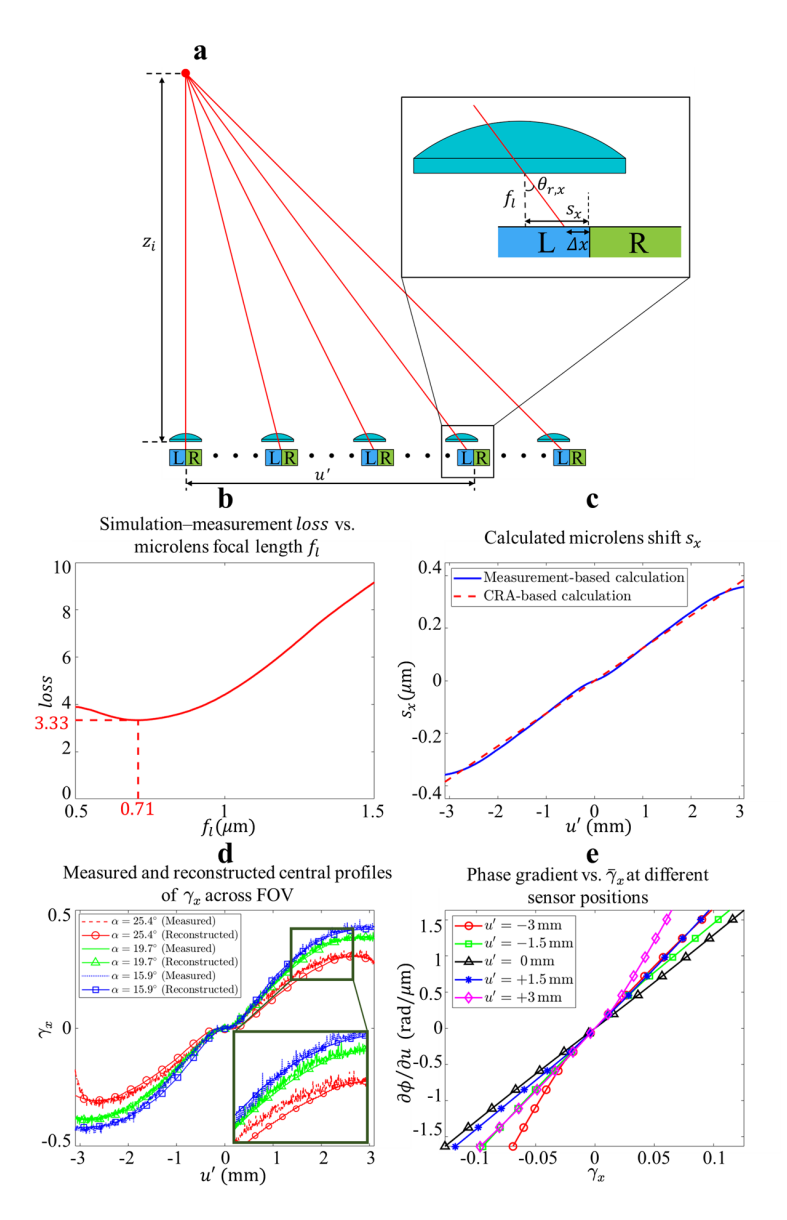


Fig. 4. Results of experimental data and simulations. (a) Geometric relationship between the microlens focal length f_l , local chief ray angle $\theta_{r,x}$, focal spot displacement Δx , and microlens shift s_x . The red ray represents the ray passing through the center of the exit pupil of the imaging system. Due to CRA mismatch, the ray does not fall onto the center of the pixel group. (b) Loss as a function of the microlens focal length $f_l=0.71~\mu m$. (c) Comparison of the microlens shift s_x calculated from the sensor CRA with that obtained from the measured data. (d) Comparison of the differential signal γ_x between measured data and reconstructed curves at different incident angles α by applying the calculated microlens shift s_x . (e) Relationship between the phase gradient $\partial \phi/\partial u$ and normalized differential signal $\bar{\gamma}_x$ at different sensor positions, obtained from simulations under the conditions $f_l=0.71~\mu m$ and $\alpha=26^\circ$, scaled by a calibration factor of 0.5

to various refractive index differences. The agreement between the theoretical phase and the reconstructed phase of microbeads immersed in all different media degraded with increasing illumination coherence. Theoretically, higher coherence leads to stronger diffraction, which distorts the reconstructed phase structure of the microbead, and this effect becomes more pronounced at larger refractive index contrasts. In addition, high coherence can lead to significant artifacts from coherent scattering by out-of-plane structures [9]. These results indicate that using lower-coherence illumination is beneficial for achieving more reliable phase detection, provided that the coherence length remains larger than the size of the 2×2 pixel group, which ensures repeatability of the phase measurement.

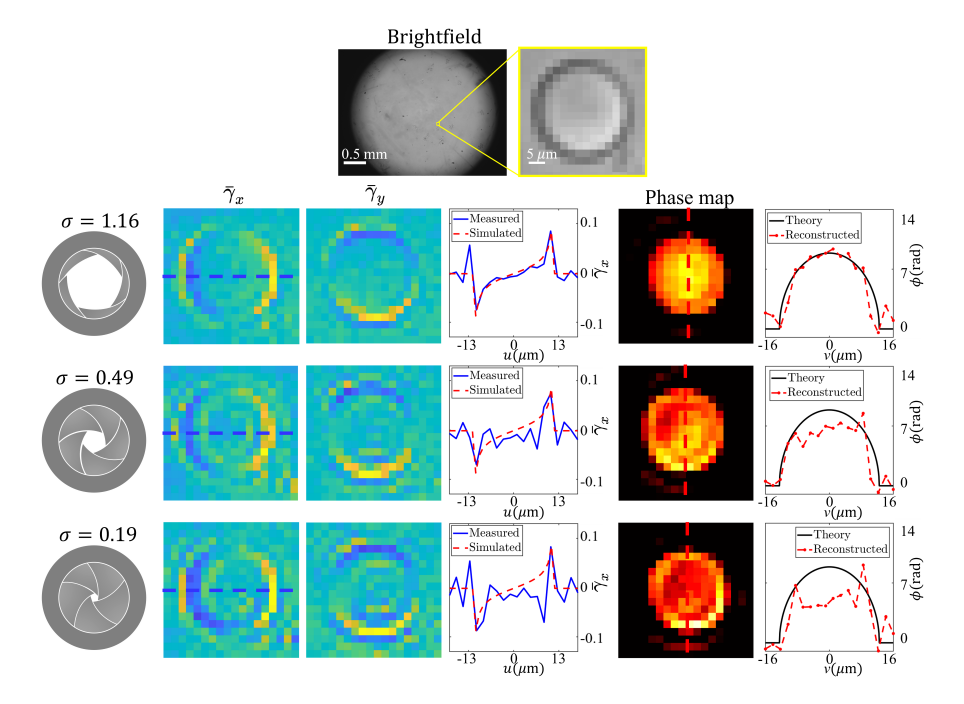


Fig. 5. Experimental results of microbeads captured at the center FOV of the sensor under different illumination coherence parameters σ . The grayscale image at the top shows a representative bright-field image obtained by binning all pixels within each 2×2 pixel group under the same microlens, along with the corresponding color channels. All microbeads were made from the same material, with an average diameter of 25 μ m and a refractive index of n_s = 1.59. The illumination coherence parameters for the three rows below are 1.16, 0.49, and 0.19, respectively. The simulated normalized differential signals shown by the blue line are scaled by a calibration factor of 0.5 with respect to the original simulated results.

Fig. 6 shows the reconstructed phase gradients at different positions on the sensor. As indicated in Fig. 4e, the same phase gradient is expected to produce smaller $\bar{\gamma}_x$ and $\bar{\gamma}_y$ values at positions farther from the sensor center along their corresponding directions. The detailed distributions of normalized differential signals of the microbeads shown in Fig. 6 are provided in supplementary Fig. S2, which verify this trend. The phase gradients used for phase reconstruction are thus estimated based on the relationship presented in Fig. 4e at the corresponding positions. The experimental results show that the sensor maintains relatively strong stability in phase-gradient measurements at positions away from the central FOV, and the reconstructed phase maps still preserve a sphere-like profile.

Fig. 7 shows an image of a mushroom slide (Coprinus c.s.) and the corresponding phase

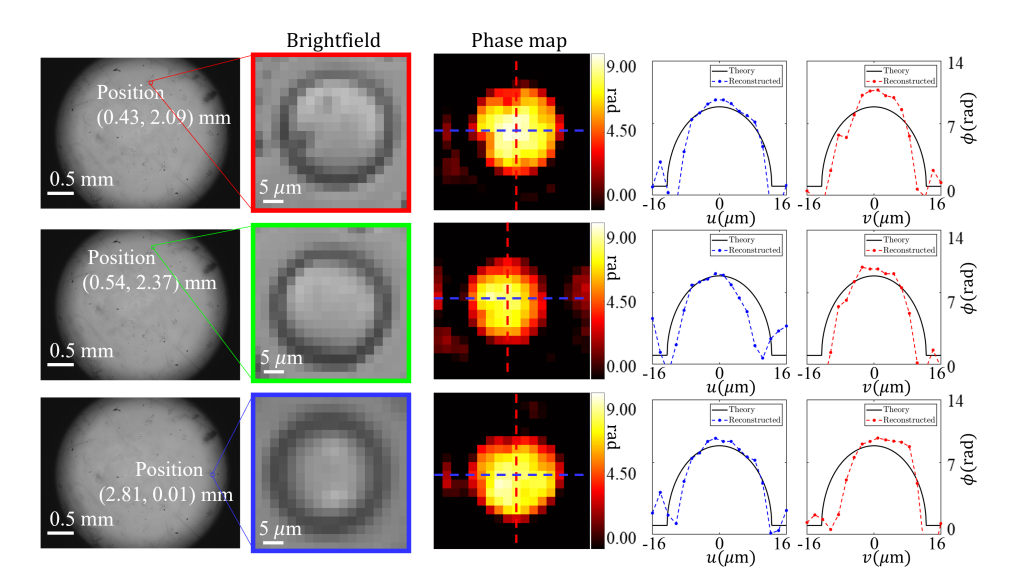


Fig. 6. Reconstructed phase maps of the microbeads ($n_s = 1.59$) captured at different positions of the imaging FOV. The image is acquired under a coherence parameter $\sigma = 1.16$ with an environmental refractive index $n_0 = 1.56$. The microbead positions are indicated on the left, with the central pixel defined as the origin. The bright-field images are generated by binning all pixels within each 2×2 pixel group under the same microlens and combining all color channels.

reconstruction obtained by QP²GI with the setup configured as in Fig. 3a. Each gill (*lamella*) of the sample contains small, ellipsoidal basidiospores (\sim 10 μ m in size), which are suitable for analyzing the phase gradients in both the horizontal and vertical directions.

For each region, the normalized differential signal is obtained by subtracting the background from the measured differential signal. The background is estimated by applying an average filtering to the original differential signals in Eq. (6), using a kernel size of 17. The reconstructed phase maps in both the central region (blue box) and the region deviating from the center (green box) reveal the structural features of the basidiospores. However, as shown in Fig. 3c, the background becomes larger and more nonlinear at positions farther from the center, making it increasingly difficult to remove. Such background not only leads to degradation of the reconstructed phase map but also reduces the reliable phase detection range, since the focal-spot shift under each microlens should remain within the valid region. This highlights the importance of achieving better CRA matching between the optical system and the sensor, which can reduce position-dependent background variations, mitigate artifacts in normalized differential signals, and ultimately improve the accuracy of phase reconstruction across the entire FOV.

4. Conclusion

In this work, we demonstrate QP²GI, a single-shot quantitative phase imaging technique using a commercially available quad-pixel PDAF sensor and simple partially coherent LED illumination. We have established a propagation model based on 2×2 pixel groups covered by a microlens and evaluated its suitability for microscopic systems. Theoretically, the maximum measurable phase gradient is jointly constrained by the numerical aperture (NA) of the imaging system and by the microlens aperture corresponding to its 2×2 pixel group. Although each sub-aperture used for phase detection is smaller than that of a traditional Shack–Hartmann wavefront sensor (typically $100-300 \ \mu m$ [29,36]), the quad-pixel PDAF sensor benefits from a much shorter distance between

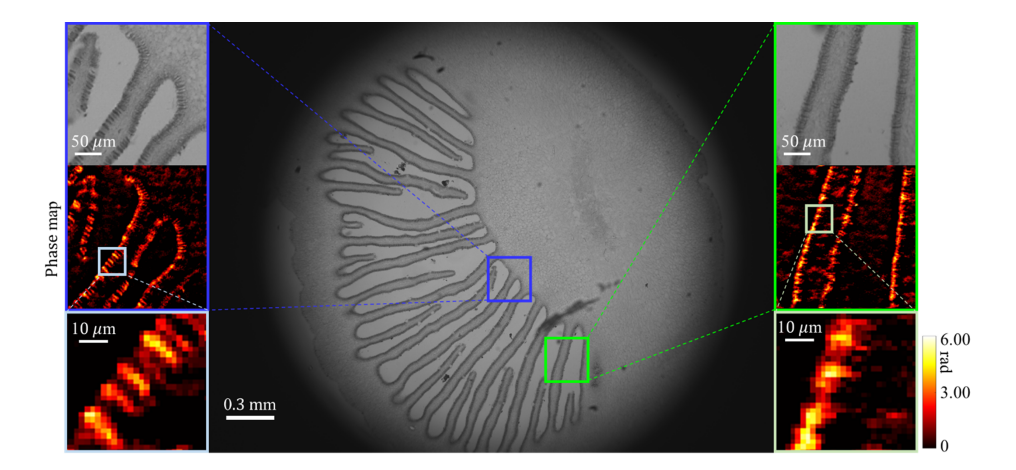


Fig. 7. Microscopic image and reconstructed phase map of a mushroom slice (*Coprinus* c.s.). The image is acquired under a coherence parameter $\sigma=1.16$. The central image presents the bright-field image, generated by binning all pixels within each 2×2 pixel group under the same microlens and combining all color channels. The blue box highlights the region near the center of the imaging FOV, while the green box indicates the region deviating from the center.

the microlens and the photosensitive layer, which allows for a potentially broader measurable range of phase gradient. Importantly, the single-shot acquisition capability of QP²GI enables quantitative phase imaging at the full frame rate of the sensor, offering a path toward high-speed, dynamic phase imaging. This is particularly advantageous for capturing rapid biological processes such as cell dynamics and intracellular transport, which are often challenging to observe with multi-frame or scanning-based QPI methods. By leveraging the native architecture of quad-pixel PDAF sensors, QP²GI could further extend the dynamic imaging capability of QPI [37, 38], particularly in applications requiring high temporal resolution. Moreover, by capturing a rapid sequence of frames at different focal planes, the quad-pixel PDAF sensor may also enable high-speed three-dimensional quantitative phase imaging. The phase-gradient maps obtained at different focal depths can be combined through computational three-dimensional reconstruction algorithms [39,40] to recover volumetric refractive-index distributions, thereby extending QP²GI from two-dimensional phase mapping to rapid volumetric phase imaging of dynamic biological processes.

The sensor performs better under relatively low coherence ($\sigma=1.16$), which suppresses artifacts associated with high coherence. The phase map of a 25 μ m microbead with a refractive index contrast of $\Delta n=0.03$ at $\sigma=1.16$ can be reconstructed with reasonable precision from a single acquisition. Both theoretical and experimental analyses confirm that phase detection remains repeatable as long as the coherence length is sufficiently larger than the size of a 2 × 2 pixel group.

The sensor's ability to detect phase gradients also degrades in regions farther from the sensor center due to CRA mismatch. Notably, the experimental results still show relatively stable phase detection in peripheral regions. Such robustness is likely because the focal spot projected onto each 2×2 pixel group is larger in practice than predicted by simulation. A larger focal spot reduces the variance in the normalized intensity difference across pixels as the spot position shifts, thereby decreasing the sensor's sensitivity to phase gradients but extending the measurable range and improving the robustness of phase detection in peripheral regions. This also explains why the simulated differential signals must be scaled by a factor of 0.5 to match the experimental

results. A more accurate simulation would require detailed knowledge of the microlens geometry and arrangement.

For biological samples with finer structures, such as *Coprinus* (c.s.), which contains small, ellipsoidal basidiospores, the reconstructed phase maps still preserve the overall structural features of the sample's phase. However, the reconstruction quality deteriorates in peripheral regions, where CRA mismatch leads to larger and more nonlinear background variations. This highlights the importance of CRA matching between the sensor and the imaging system to ensure reliable phase measurements.

Multi-camera array microscopes (MCAM) [41,42], which employ high-NA finite-conjugate lenses with relatively low magnification (0.1–0.3) to maintain overlap between each sub-FOV, inherently require relatively large CRA. This makes them strong candidates for integration with such sensors. In addition, CRA matching between the optical system and the sensor may be further improved through the use of a relay lens, which modifies the chief-ray distribution at the sensor plane and offers a practical route to enhanced phase measurement accuracy in microscopic systems employing this type of sensor.

Another potential approach is to design a quad-pixle PDAF sensor with minimal intentional microlens shift, thereby achieving intrinsic CRA matching to microscope systems with small CRA through sensor architecture. In this configuration, the optical axis of each microlens aligns with that of the imaging system, effectively eliminating CRA-induced phase detection bias and simplifying system calibration, thus offering a more robust and inherently compatible platform for QP²GI.

Funding.

This work was not supported by any funding agency.

Disclosures.

X.B. was a student at Duke University during this work and is currently employed by Ramona Optics, Inc. R.H. is both a faculty member at Duke University and a co-founder of Ramona Optics, Inc. The remaining authors declare no conflicts of interest.

Data availability.

The data that support the findings of this study are available upon reasonable request from the authors.

Supplemental document.

See Supplement 1 for supporting content.

References

- T. L. Nguyen, S. Pradeep, R. L. Judson-Torres, et al., "Quantitative Phase Imaging: Recent Advances and Expanding Potential in Biomedicine," ACS Nano 16, 11516–11544 (2022).
- H. Majeed, S. Sridharan, M. Mir, et al., "Quantitative phase imaging for medical diagnosis," J. Biophotonics 10, 177–205 (2017).
- Z. Huang and L. Cao, "Quantitative phase imaging based on holography: trends and new perspectives," Light Sci Appl 13, 145 (2024). Publisher: Nature Publishing Group.
- C. J. Mann, L. Yu, C.-M. Lo, and M. K. Kim, "High-resolution quantitative phase-contrast microscopy by digital holography," Opt. Express 13, 8693–8698 (2005).
- C. J. Sheppard, "Defocused transfer function for a partially coherent microscope and application to phase retrieval," J. Opt. Soc. Am. A 21, 828–831 (2004).
- Y. Bao and T. K. Gaylord, "Two improved defocus quantitative phase imaging methods: discussion," J. Opt. Soc. Am. A 36, 2104–2114 (2019).
- Y.-Z. Lin, K.-Y. Huang, and Y. Luo, "Quantitative differential phase contrast imaging at high resolution with radially asymmetric illumination," Opt. Lett. 43, 2973–2976 (2018).
- Y. Fan, J. Sun, Q. Chen, et al., "Optimal illumination scheme for isotropic quantitative differential phase contrast microscopy," Photon. Res. 7, 890–904 (2019).
- L. Tian and L. Waller, "Quantitative differential phase contrast imaging in an LED array microscope," Opt. Express 23, 11394–11403 (2015).
- D. K. Hamilton, C. J. R. Sheppard, and T. Wilson, "Improved imaging of phase gradients in scanning optical microscopy," J. Microsc. 135, 275–286 (1984).

- G. Zheng, R. Horstmeyer, and C. Yang, "Wide-field, high-resolution fourier ptychographic microscopy," Nat. Photonics 7, 739–745 (2013).
- X. Ou, R. Horstmeyer, C. Yang, and G. Zheng, "Quantitative phase imaging via fourier ptychographic microscopy," Opt. Lett. 38, 4845–4848 (2013).
- M. Levoy, R. Ng, A. Adams, et al., "Light field microscopy," in ACM SIGGRAPH 2006 Papers, (ACM Press, 2006), p. 924.
- M. Broxton, L. Grosenick, S. Yang, et al., "Wave optics theory and 3-D deconvolution for the light field microscope," Opt. Express 21, 25418–25439 (2013).
- 15. O. Bimber and D. Schedl, "Light-field microscopy: A review," J. Neurol. Neuromed. 4, 1-6 (2019).
- L. Mignard-Debise and I. Ihrke, "Light-field microscopy with a consumer light-field camera," in 2015 International Conference on 3D Vision, (2015), pp. 335–343.
- B. C. Platt and R. Shack, "History and Principles of Shack-Hartmann Wavefront Sensing," J. Refract. Surg. 17, S573–S577 (2001).
- R. G. Lane and M. Tallon, "Wave-front reconstruction using a Shack-Hartmann sensor," Appl. Opt. 31, 6902–6908 (1992).
- 19. J. Primot, "Theoretical description of Shack-Hartmann wave-front sensor," Opt. Commun. 222, 81-92 (2003).
- 20. P. M. Prieto, F. Vargas-Martín, S. Goelz, and P. Artal, "Analysis of the performance of the Hartmann–Shack sensor in the human eye," J. Opt. Soc. Am. A 17, 1388–1398 (2000).
- 21. X. Wei and L. Thibos, "Design and validation of a scanning Shack Hartmann aberrometer for measurements of the eye over a wide field of view," Opt. Express 18, 1134–1143 (2010).
- T. M. Jeong, M. Menon, and G. Yoon, "Measurement of wave-front aberration in soft contact lenses by use of a Shack–Hartmann wave-front sensor," Appl. Opt. 44, 4523–4527 (2005).
- R. M. Abdelazeem, M. M. A. Ahmed, and M. Agour, "Characterization of thick and contact lenses using an adaptive Shack-Hartmann wavefront sensor: Limitations and solutions," Optik 283, 170922 (2023).
- D. Dayton, B. Pierson, B. Spielbusch, and J. Gonglewski, "Atmospheric structure function measurements with a Shack-Hartmann wave-front sensor," Opt. Lett. 17, 1737–1739 (1992).
- 25. K. Kikuchi, K. Tomioka, T. Usui, *et al.*, "A 1.25 μm, 59.3 mpixel, 60 fps cmos image sensor with 2×1 multi-directional phase-detection pixels," in 2024 IEEE SENSORS, (2024), pp. 1–4.
- 26. K. Fukuda, "A compressed $n \times n$ multi-pixel imaging and cross phase-detection af with $n \times 1$ rgrb + $1 \times$ ngb hetero multi-pixel image sensors," in *Proc. Int. Image Sensor Workshop*, (2021), p. R28.
- 27. "OV50A," https://www.ovt.com/products/ov50a/.
- S. Jutamulia, "Phase detection autofocus (PDAF) image sensor as applied to 3D imaging," J. Physics: Conf. Ser. 2274, 012005 (2022).
- D. R. Neal, J. Copland, and D. A. Neal, "Shack-Hartmann wavefront sensor precision and accuracy," in *Advanced Characterization Techniques for Optical, Semiconductor, and Data Storage Components*, vol. 4779 (Seattle, WA, 2002), pp. 148–160.
- 30. S. Thomas, T. Fusco, A. Tokovinin, *et al.*, "Comparison of centroid computation algorithms in a Shack–Hartmann sensor," Mon. Notices Royal Astron. Soc. **371**, 323–336 (2006).
- 31. J. W. Goodman, Statistical Optics (John Wiley & Sons, 2015).
- 32. A. Taflove, S. C. Hagness, and M. Piket-May, "Computational electromagnetics: the finite-difference time-domain method," The Electr. Eng. Handb. 3, 15 (2005).
- 33. R. Frankot and R. Chellappa, "A method for enforcing integrability in shape from shading algorithms," IEEE Trans. on Pattern Anal. Mach. Intell. 10, 439–451 (1988).
- S. Holland, N. Wang, and W. Moses, "Development of low noise, back-side illuminated silicon photodiode arrays," IEEE Trans. on Nucl. Sci. 44, 443–447 (1997).
- 35. G. Taverni, D. Paul Moeys, C. Li, *et al.*, "Front and back illuminated dynamic and active pixel vision sensors comparison," IEEE Trans. on Circuits Syst. II: Express Briefs **65**, 677–681 (2018).
- 36. R. K. Tyson and B. W. Frazier, Principles of Adaptive Optics (CRC Press, 2022), 5th ed.
- 37. C. P. Casteleiro, B. Wang, C. E. Serafini, et al., "Functional imaging with dynamic quantitative oblique backillumination microscopy," J. Biomed. Opt. 27, 066502 (2022).
- 38. A. Krizova, J. Collakova, Z. Dostal, *et al.*, "Dynamic phase differences based on quantitative phase imaging for the objective evaluation of cell behavior," J. Biomed. Opt. **20**, 111214 (2015).
- M. H. Jenkins and T. K. Gaylord, "Three-dimensional quantitative phase imaging via tomographic deconvolution phase microscopy," Appl. Opt. 54, 9213–9227 (2015).
- 40. M. Chen, L. Tian, and L. Waller, "3d differential phase contrast microscopy," Biomed. Opt. Express 7, 3940–3950 (2016)
- 41. M. Harfouche, K. Kim, K. C. Zhou, *et al.*, "Imaging across multiple spatial scales with the multi-camera array microscope," Optica **10**, 471–480 (2023).
- 42. L. Kreiss, W. Tang, R. Balla, *et al.*, "Recording dynamic facial micro-expressions with a multi-focus camera array," Biomed. Opt. Express **16**, 617–627 (2025).

Towards a mobile quantitative phase imaging microscope with smartphone phase-detection sensors

Supplement 1

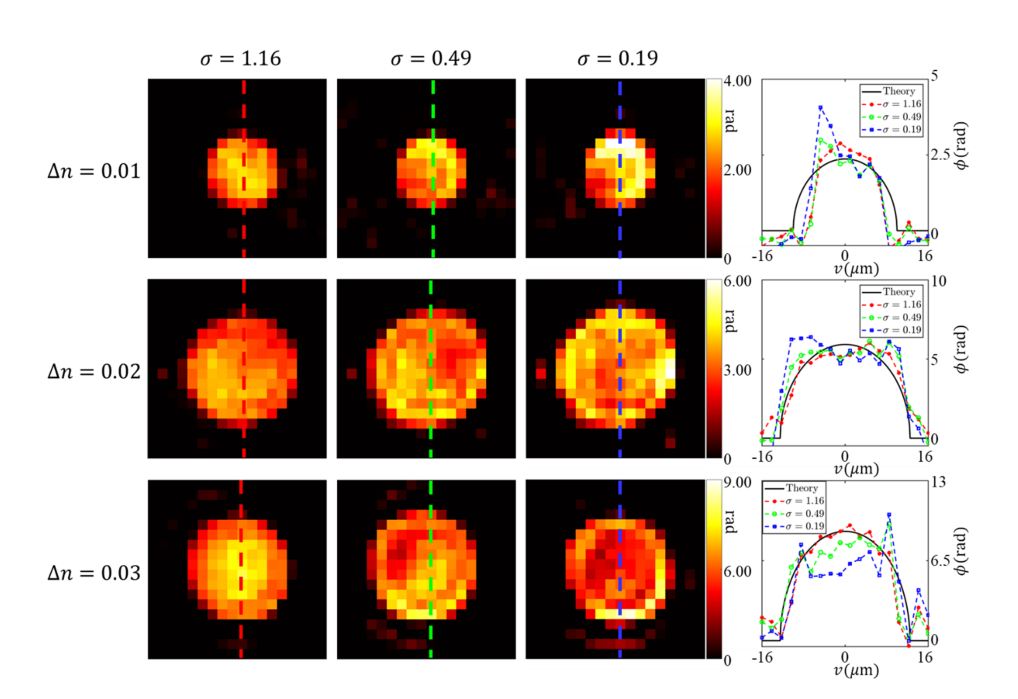


Fig. S1. Reconstructed phase maps of the microbeads (refractive index $n_s = 1.59$) captured at the central field of view (FOV). The microbeads (nominal diameter = 25 μ m) are immersed in environments with refractive indices $n_0 = 1.58$, 1.57, and 1.56, respectively. The results shown in each row are reconstructed from the same microbead, acquired under identical conditions except for the illumination coherence. The microbead in the $n_0 = 1.58$ medium exhibits a slightly smaller actual diameter of $\sim 22 \ \mu$ m. Illumination with coherence parameters $\sigma = 1.16$, 0.49, and 0.19 is applied during imaging. The coherence parameter is defined as the ratio of the illumination numerical aperture to the objective numerical aperture. The rightmost column shows the central profiles of the reconstructed phase compared with the corresponding theoretical predictions.

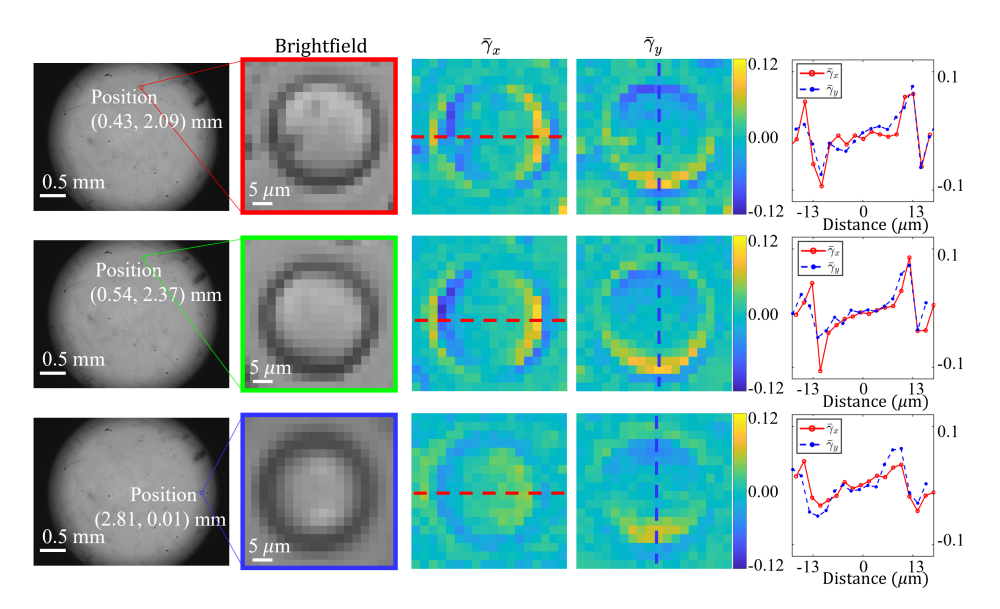


Fig. S2. Normalized differential signals $\bar{\gamma}_x$ and $\bar{\gamma}_y$ of the microbeads ($n_s = 1.59$) captured at different positions of the imaging FOV. The images are acquired under a coherence parameter $\sigma = 1.16$ with an environmental refractive index of $n_0 = 1.56$. The positions of the microbeads are indicated in the left column, with the central pixel defined as the origin. The rightmost column shows the central profiles of the normalized differential signals for microbeads located at different sensor positions.